

## Sea surface current estimation using optical satellite imagery of Kelvin wakes and AIS data

Haakman, Koen; Verlaan, Martin; Gerritsma, Avelon; van der Hout, Arne

**DOI**

[10.1016/j.rse.2024.114400](https://doi.org/10.1016/j.rse.2024.114400)

**Publication date**

2024

**Document Version**

Final published version

**Published in**

Remote Sensing of Environment

**Citation (APA)**

Haakman, K., Verlaan, M., Gerritsma, A., & van der Hout, A. (2024). Sea surface current estimation using optical satellite imagery of Kelvin wakes and AIS data. *Remote Sensing of Environment*, 315, Article 114400. <https://doi.org/10.1016/j.rse.2024.114400>

**Important note**

To cite this publication, please use the final published version (if applicable). Please check the document version above.

**Copyright**

Other than for strictly personal use, it is not permitted to download, forward or distribute the text or part of it, without the consent of the author(s) and/or copyright holder(s), unless the work is under an open content license such as Creative Commons.

**Takedown policy**

Please contact us and provide details if you believe this document breaches copyrights. We will remove access to the work immediately and investigate your claim.



# Sea surface current estimation using optical satellite imagery of Kelvin wakes and AIS data

Koen Haakman<sup>a,b,\*</sup>, Martin Verlaan<sup>a,c</sup>, Avelon Gerritsma<sup>c</sup>, Arne van der Hout<sup>a,b</sup>

<sup>a</sup> Delfares, Delft, The Netherlands

<sup>b</sup> Department of Civil Engineering and Geosciences, TU Delft, Delft, The Netherlands

<sup>c</sup> Department of Electrical Engineering, Mathematics and Computer Science, TU Delft, Delft, The Netherlands

## ARTICLE INFO

Edited by Menghua Wang

### Keywords:

Surface currents

Kelvin wake

Optical satellite imagery

Sentinel-2

Generalized radon transform

AIS

## ABSTRACT

Sea surface currents are of significant importance in various scientific and maritime applications. There are several measurement techniques available to study surface currents, however, they have limitations in spatial coverage and resolution. This study presents a proof-of-concept for a new measurement principle that relies on the difference between a ship's speed relative to water and land. The approach involves estimating the ship speed vector relative to water from optical satellite imagery of Kelvin wakes. This ship speed vector is subtracted from the ship speed over ground, which is determined from Automatic Identification System (AIS) data, to estimate the surface current. A case study in the Strait of Gibraltar was performed using two months of Sentinel-2 imagery, which yielded 81 visible Kelvin wakes over 25 images. Surface currents were estimated in directions parallel and perpendicular to the ship's sailing line for each Kelvin wake. The estimated currents were validated with respect to surface currents derived from High-Frequency Radars (HFRs) and modelled currents from the Copernicus Marine Environmental Monitoring Service (CMEMS). The uncertainty in the two surface current components was estimated using triple collocation. After removing 12 data points with large ship course variability, standard deviations of 0.14 and 0.16 m s<sup>-1</sup> were estimated for the surface currents along and across the sailing line, respectively. Despite limitations in measurement frequency due to satellite revisit times, cloud cover and Kelvin wake visibility, this new method can provide accurate estimates of sea surface currents in regions with high vessel density.

## 1. Introduction

Sea surface currents are important for many scientific and maritime applications. These currents influence weather and climate; water levels; transport of energy, sediment and pollutants; shipping routes and fish distribution, among others. Accurate measurements of surface currents are crucial to our understanding of physical processes, but also for the development of hydrodynamic models. However, present-day measurement techniques are still unsatisfactory in spatial resolution and coverage (Isern-Fontanet et al., 2017).

In-situ measurements provide excellent temporal resolution, but their number is too few to provide good spatial resolution. While High-Frequency Radars (HFRs) achieve good spatial and temporal resolution, their spatial coverage is limited to a few coastal sites. Surface drifters provide a great dataset to study surface currents globally (e.g., Lumpkin et al. (2017)), however, at any given time, there are generally little to no drifters in specific marginal seas. Therefore, their use in regions with significant human activity is limited.

There also exist several remote sensing techniques for estimating ocean currents, as discussed in e.g. Klemas (2012) and Hauser et al. (2023). The estimation of geostrophic currents through satellite altimetry has been successful, but altimetry is challenging in coastal regions due to large footprints and insufficiently accurate geophysical corrections. Moreover, in coastal areas, currents may deviate significantly from the geostrophic balance.

Surface currents have also been estimated from Synthetic Aperture Radar (SAR) imagery using two techniques: Along-Track Interferometry (ATI) (e.g. Romeiser et al., 2010) and Doppler Centroid Anomaly estimation (DCA) (Chapron et al., 2005). In ATI, the phase difference between two SAR images captured with a small time lag is related to the surface current. In DCA, the Doppler shift of the radar echoes is analysed to detect a contribution of the surface current. Main limitations of these techniques include inaccurate removal of wave effects and that they provide only the radar line-of-sight component of the

\* Corresponding author at: Department of Civil Engineering and Geosciences, TU Delft, Delft, The Netherlands.

E-mail address: [k.b.haakman@tudelft.nl](mailto:k.b.haakman@tudelft.nl) (K. Haakman).

<https://doi.org/10.1016/j.rse.2024.114400>

Received 27 January 2024; Received in revised form 20 August 2024; Accepted 27 August 2024

Available online 9 September 2024

0034-4257/© 2024 The Author(s). Published by Elsevier Inc. This is an open access article under the CC BY license (<http://creativecommons.org/licenses/by/4.0/>).

surface current (Hauser et al., 2023). Hence, additional assumptions are required to project these into East and North components.

The reconstruction of total surface currents is one of the objectives of the Harmony Earth Explorer 10 mission. This will be achieved by measuring radar echoes transmitted by Sentinel-1 using two new satellites carrying receive-only radars (López-Dekker et al., 2019). This allows the estimation of radial surface currents with three lines of sight, which enables computation of the total surface current. However, the launch of these satellites is not expected before 2029.

Optical satellite imagery has also been used to derive surface currents by exploiting the small inter-band time lags of the Sentinel-2 MultiSpectral Instrument (MSI) (Yurovskaya et al., 2019). They compute phase shifts between the spectra generated from the blue and red image bands, which have a time lag of about 1 s. After removing the phase shift predicted from the linear dispersion relation, the remaining phase shift is attributed to the surface current. The method shows promising results and is able to achieve good spatial resolution and coverage. Still, the method has limitations including cases where waves and currents are nearly perpendicular, errors due to inaccurate co-registration and difficulty in estimating small currents due to the short time lag between the high-resolution MSI bands.

Recently, data from the Automatic Identification System (AIS) has also been used to estimate surface currents (Le Goff et al., 2021; Christodoulou et al., 2022; Yiew and Magee, 2022). The AIS is a maritime collision-avoidance system in which ships transmit their position, speed over ground, course over ground and true heading, among others. Le Goff et al. (2021) demonstrate that surface currents can be estimated by subtracting a ship's speed through water from its speed over ground. However, since the speed through water is not measured by a ship, it cannot be broadcast through AIS. Le Goff et al. (2021) circumvent this problem by combining data from multiple ships within a spatiotemporal interval, and including each ship's speed through water as an unknown in the estimation problem. As a result, the temporal and spatial resolution are reduced and depend on ship density. Moreover, an error is introduced as the flow field need not be homogeneous within such a spatiotemporal interval.

In deep water, a ship's speed through water uniquely determines the wavelength pattern in the ship's Kelvin wake (Gomit et al., 2014; Sun et al., 2018). A Kelvin wake is the V-shaped wave pattern generated by a moving pressure distribution, such as a ship. Therefore, by determining the wavelengths in a Kelvin wake, the speed of a ship through water can be estimated (Tunaley, 2003; Zilman et al., 2004; Graziano et al., 2016a,b). By subtracting this variable from the speed over ground of the vessel obtained from AIS data, surface currents can be estimated using data from a single ship, as opposed to having to aggregate data from multiple ships. Hence, this study aims to investigate how accurate sea surface currents can be estimated by combining optical imagery of Kelvin wakes with AIS data.

A more detailed explanation of the new measurement principle is given in the next section. Thereafter, a spectral model for a Kelvin wake, based on linear wave theory, is given. Section 3 presents an algorithm to retrieve the ship speed and course relative to water from optical imagery of Kelvin wakes. In Section 4, the data and methods for a case study in the Strait of Gibraltar are given. The results of this case study are presented in Section 5. Finally, the discussion and conclusions are given in Section 6.

## 2. Theory

### 2.1. Measurement principle

The measurement principle is based on the fact that for a given ship, the ship speed can be defined in two frames of reference. First, the ship speed can be defined relative to stationary land. The corresponding magnitude and direction are referred to as the Speed Over Ground (SOG) and Course Over Ground (COG), respectively. For brevity, we

will denote these variables with  $V_g, \theta_g$ , with the subscript  $g$  for ground. Second, the ship speed can be defined relative to the surrounding current. The Speed Through Water (STW) and Course Through Water (CTW) represent the magnitude and direction of this ship speed vector. They will be denoted with  $V_w$  and  $\theta_w$ , where  $w$  represents water. The difference between the two ship speed vectors is the surface current at the ship's location. Hence, the current can be computed as the vector difference of two independent ship speed vectors. In Fig. 1, the geometrical relationship between the two ship speed vectors and the surface current vector is visualized.

From Fig. 1, equations for the components of the current along and across the sailing line can be derived:

$$U_{\text{along}} = V_g \cos(\theta_w - \theta_g) - V_w, \quad (1)$$

$$U_{\text{across}} = V_g \sin(\theta_w - \theta_g). \quad (2)$$

Eqs. (1) and (2) contain four unknowns. Two of these unknowns,  $V_g$  and  $\theta_g$ , can be obtained from AIS data. The ship course through water,  $\theta_w$ , cannot be reliably estimated by a ship's True Heading, although this variable is contained in the AIS data, since the heading of the ship may be influenced by crosswinds. However,  $\theta_w$  can be determined from the orientation of a Kelvin wake on optical imagery. Finally,  $V_w$  is related to the wavelengths in the Kelvin wake, with faster ships generating longer waves. In the present study, we will use Sentinel-2 imagery to estimate  $V_w$  and  $\theta_w$ .

### 2.2. Spectral representation Kelvin wake

Following Gomit et al. (2014), the relationship between  $V_w$  and the wavelengths in a Kelvin wake can be derived from the linear dispersion relation for surface gravity waves in deep water, i.e.,

$$\omega^2 = gk, \quad (3)$$

where  $\omega$  is the angular frequency of a wave,  $g$  is the gravitational acceleration and  $k = \sqrt{k_x^2 + k_y^2}$  denotes the wavenumber. Now suppose that the reference frame is fixed to the ship, with the  $x$ -axis aligning with the sailing line. Then, the reference frame moves with a constant speed  $V_w$ . This introduces a Doppler-shifted apparent frequency that is given by

$$\omega' = \omega - V_w k_x, \quad (4)$$

where  $\omega'$  is the angular frequency in the moving frame of reference. Substitution of Eq. (4) into Eq. (3) gives

$$(\omega' + V_w k_x)^2 = gk. \quad (5)$$

We assume that the Kelvin waves are stationary with respect to the ship, hence  $\omega' = 0$ . Then, Eq. (5) reduces to

$$V_w = \pm \frac{\sqrt{gk}}{k_x}. \quad (6)$$

As the Kelvin waves are travelling in the same direction as the ship, the negative solution can be ignored. The above expression can be reordered to obtain an equation for the spectral shape of a Kelvin wake:

$$k_y = \pm k_x \sqrt{\frac{V_w^4}{g^2 k_x^2} - 1}. \quad (7)$$

This equation describes the shape of the Kelvin wave pattern in the spectral domain and it represents the model that will be fit to observed data. In Fig. 2a, the model is shown for three different values of a ship's  $V_w$ . It can be seen that by increasing  $V_w$ , the model moves radially inward. This corresponds to waves becoming longer. In Fig. 2b, the model is numerically rotated to show the spectrum for a ship with  $\theta_w$  of  $45^\circ$  counter-clockwise with respect to the positive  $x$ -axis.

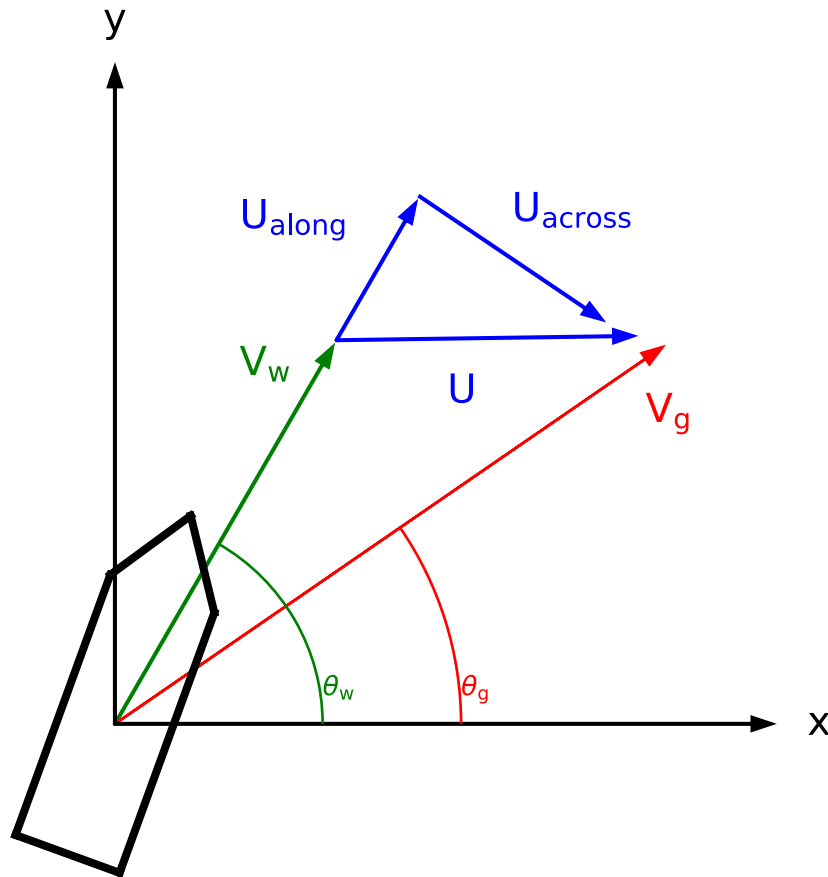


Fig. 1. Geometrical relation between the ship speed vectors and the surface current components. Note that the ship speed through water ( $V_w$ ) does not align with the true heading. The along and across components of the current are thus defined with respect to the sailing line.

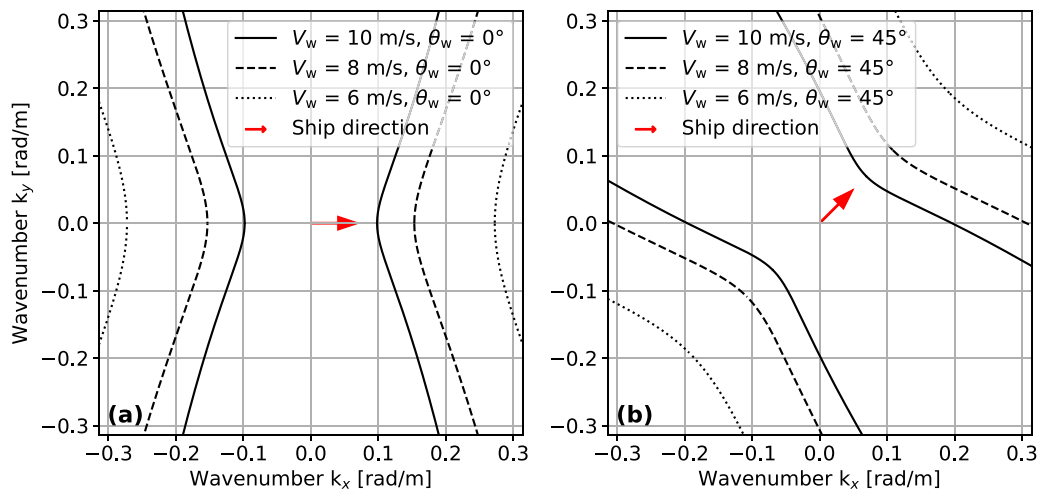


Fig. 2. (a) Theoretical shape of the Kelvin wake pattern in the spectral domain. The dotted, dashed and solid lines correspond to a ship speed through water ( $V_w$ ) of 6, 8 and 10 m/s respectively. The ship is assumed to be moving in positive  $x$ -direction, as indicated by the red arrow. (b) As in (a), but now for a ship with a heading of  $45^\circ$  counter-clockwise with respect to the positive  $x$ -axis.

### 2.3. Lower bound ship speed through water

In Fig. 2, it can be seen that as the ship speed decreases, the model moves radially outward. At some point, the model is no longer visible on the spectrum. The boundaries of the spectrum are chosen such that they correspond to the maximum wavenumber distinguishable on Sentinel-2 imagery. According to the Nyquist criterion, a wave must be sampled with at least 2 samples per wavelength to be reconstructed. For

Sentinel-2 imagery, with a ground sampling distance of 10 m, the wavelengths must be at least 20 m, resulting in a maximum wavenumber of  $2\pi/20 \approx 0.314$  rad/m.

Given the lower bound on the wavelength above, we can compute the minimum ship speed through water required to generate such a wavelength. At a given ship speed, the longest wave in a Kelvin wake is found along the sailing line, hence they have  $k_y = 0$ . This gives  $k = k_x$ ,

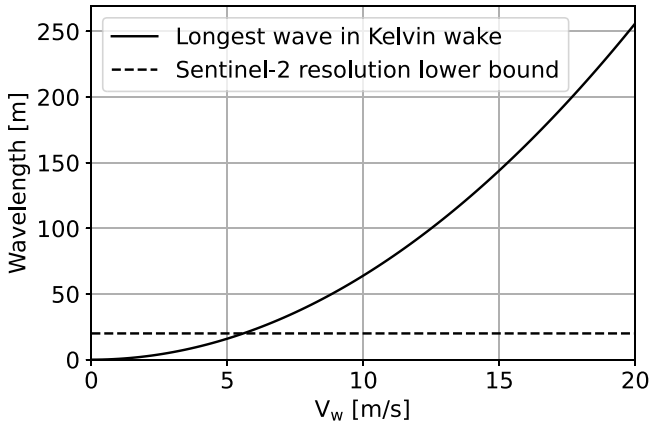


Fig. 3. Longest wavelength in the Kelvin wake as a function of the ship speed through water ( $V_w$ ) Eq. (8).

such that Eq. (7) can be reduced to

$$L_{\max} = 2\pi \frac{V_w^2}{g}, \quad (8)$$

where  $L_{\max}$  denotes the longest wavelength present in the Kelvin wake. In Fig. 3 this relationship between  $V_w$  and the longest wavelength in the Kelvin wake is shown. By substituting  $L_{\max} = 20$  m into Eq. (8), we find that the minimum  $V_w$  required for detection on Sentinel-2 imagery is about  $5.6 \text{ m s}^{-1}$ . However, this bound was computed for waves travelling along the sailing line. Waves oblique to the sailing line are shorter, hence they require a slightly larger ship speed through water to meet the minimum wavelength requirement. We observed that a ship speed through water of about  $6 \text{ m s}^{-1}$  suffices for Kelvin wake detection on Sentinel-2 imagery. For higher resolution satellite imagery, such as WorldView or SPOT, a lower ship speed should suffice.

#### 2.4. Sensitivity $U_{\text{across}}$ to ship course

The estimates for  $U_{\text{across}}$  are very sensitive to small deviations in a ship's course. This can be seen by differentiating Eqs. (1) and (2) with respect to the angular difference  $\eta = \theta_g - \theta_w$ . Differentiation of both equations with respect to  $\eta$  yields

$$\frac{\partial U_{\text{along}}}{\partial \eta} = -V_g \sin(\eta), \quad (9)$$

$$\frac{\partial U_{\text{across}}}{\partial \eta} = V_g \cos(\eta). \quad (10)$$

Since  $\eta \ll 1$ ,  $\sin(\eta) \approx \eta$  and  $\cos(\eta) \approx 1 - \frac{\eta^2}{2}$ . Substitution of these approximations leads to

$$\frac{\partial U_{\text{along}}}{\partial \eta} \approx -V_g \eta, \quad (11)$$

$$\frac{\partial U_{\text{across}}}{\partial \eta} \approx V_g \left(1 - \frac{\eta^2}{2}\right). \quad (12)$$

Hence, at a speed over ground of  $10 \text{ m s}^{-1}$ , a deviation of just  $1^\circ$  in either  $\theta_g$  or  $\theta_w$  leads to a change of  $0.17 \text{ m s}^{-1}$  in  $U_{\text{across}}$ , while the change is negligible for  $U_{\text{along}}$ . This illustrates that accurate retrieval of the across-sailing-line surface current requires a stable ship course and precise estimation of the ship course through water.

### 3. Retrieval algorithm

#### 3.1. Extraction spectral Kelvin wake signal

The ship speed through water vector will be derived from the spectral Kelvin wake signal. Therefore, this signal needs to be extracted

from an image containing a Kelvin wake. To that end, we first multiply the image by a Hann window in order to reduce spectral leakage. Subsequently, its Discrete Fourier Transform (DFT) is computed. An example of a Sentinel-2 image containing a Kelvin wake and its Hann-windowed DFT is given in Fig. 4.

To further isolate the spectral Kelvin wake signal, a radial trend is subtracted from the spectrum using least-squares. Subsequently, pixel values below 0 dB are removed. In Fig. 5 an example of a filtered spectrum is given.

#### 3.2. Model fitting

Now that the spectral Kelvin wake signal is extracted, the forward model for this signal (Eq. (7)) needs to be matched to the observed spectrum. To that end, the Generalized Radon Transform (GRT) is used. The GRT of a spectrum  $S$  with coordinates  $k = (k_x, k_y)$  is given by (e.g. Luengo Hendriks et al., 2005)

$$\mathcal{R}\{S\}(p) = \int_{C_p} S(k) dk, \quad (13)$$

where  $C_p$  denotes the curve corresponding to the forward model with parameters  $p = (V_w, \theta_w)$ .

The goal of the GRT is to find the set of parameters  $p$  such that the curve  $C_p$  aligns with the Kelvin wake signal present in  $S$ . To that end, initial guesses of  $p$  are first defined. Subsequently, for each candidate set  $p$ , a line integral along  $C_p$  over  $S(k)$  is computed. In Fig. 5a, the curves  $C_p$  for three inaccurate guesses of  $p$  are shown. As can be seen, the curves do not align with the Kelvin wake signal. Therefore, the value of the line integral will be small. On the other hand, Fig. 5b shows a curve  $C_p$  for an accurate guess of  $p$ . Now, the model overlaps with the Kelvin wake signal. Therefore, the value of the line integral is large. The GRT computes the line integral over all prescribed initial guesses for  $p$ . Finally, the best fit is given by the set of parameters that maximizes the line integral.

In practice, there are only a finite number of pixels in an image. Hence, the line integral in Eq. (13) is discretized which gives

$$\mathcal{R}\{S\}(p) = \sum_{i=0}^{N-1} S(k_i), \quad (14)$$

where  $k_i$  for  $i \in \{0, N-1\}$  represent the image coordinates of the pixels located along curve  $C_p$ . However, in this application, the curves produced by the forward model have different lengths for different combinations of parameters. Hence, a bias towards longer curves may be introduced. Therefore, the GRT is modified to take the average along a curve instead of only summing the relevant pixels. This gives

$$\mathcal{R}\{S\}(p) = \frac{1}{N} \sum_{i=0}^{N-1} S(k_i). \quad (15)$$

The GRT defines a mapping from the spectral domain to a parameter domain. The parameter domain, also called the Radon domain, is spanned by  $V_w$  and  $\theta_w$ . Hence, the result of the GRT can also be shown as a 2D image. An example of this is shown in Fig. 6. Every point in this parameter domain corresponds to a combination of  $V_w$  and  $\theta_w$ . The intensity at this point is equal to the average power in the spectrum over the curve produced by this combination of parameters. Hence, a large intensity means that the model curve is overlapping with a signal in the spectral domain. Therefore, the location of the maximum in the parameter domain gives the fitted parameters, i.e.,

$$\hat{p} = (\hat{V}_w, \hat{\theta}_w) = \underset{p}{\operatorname{argmax}} \mathcal{R}\{S\}(p). \quad (16)$$

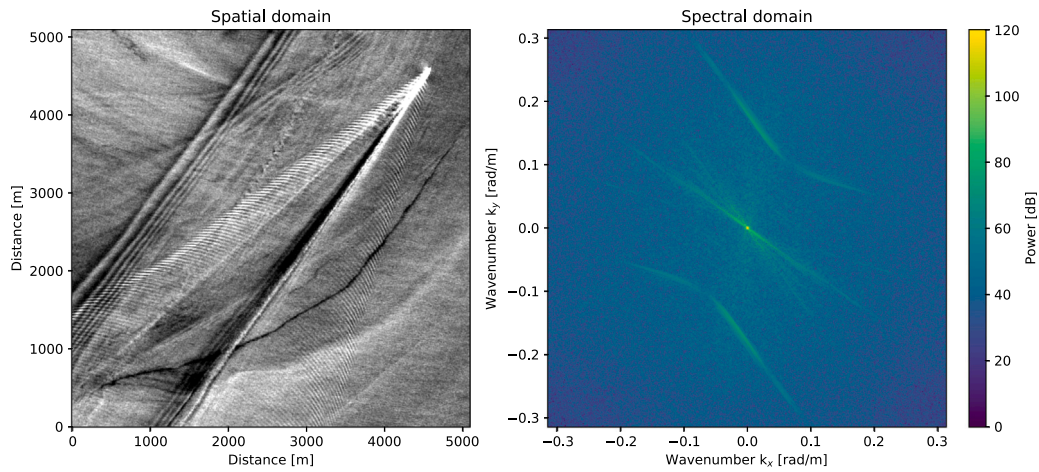


Fig. 4. Example of a Sentinel-2 image of a Kelvin wake (left) and its Hann-windowed Discrete Fourier transform (right).

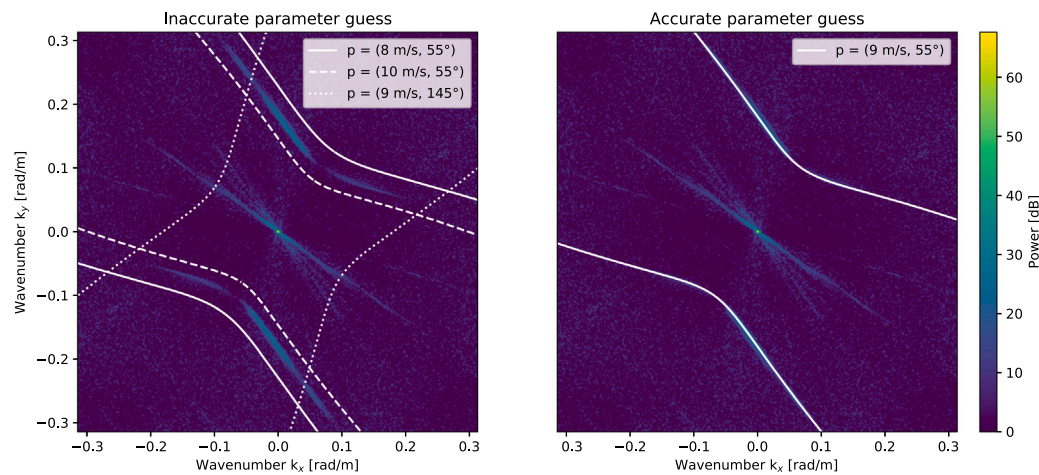


Fig. 5. (a) Examples of inaccurate guesses of the parameter set  $p$  that yield model curves  $C_p$  which do not align with the Kelvin wake signal. (b) Example of accurate guess of the parameter set  $p$  yielding a model curve that lines up with the observed curve.

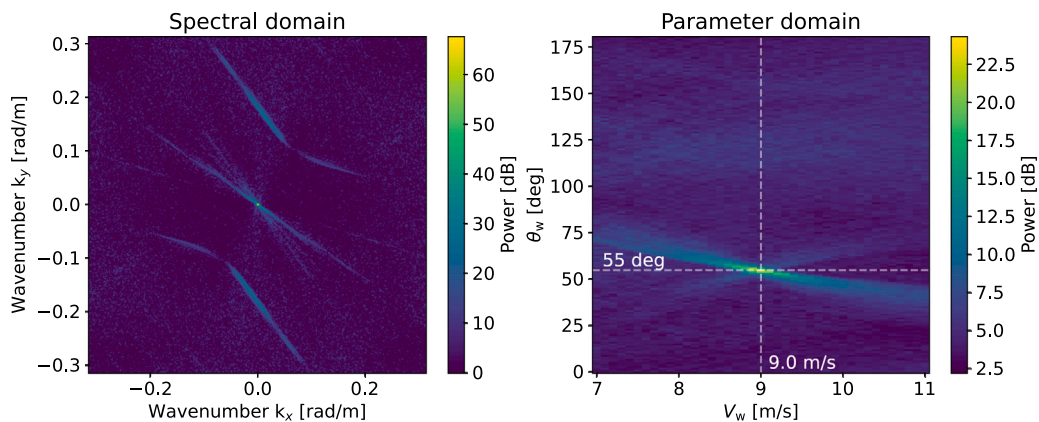


Fig. 6. (a) Filtered Fourier spectrum of windowed Sentinel-2 Kelvin wake image. (b) Generalized Radon Transform of (a), normalized to a scale from zero to unity.

### 3.3. Convergence angle correction

A direction measured in a given map projection is generally not equal to the direction in a different map projection. Since  $\hat{\theta}_w$  is measured in a Sentinel-2 image, it is a direction with respect to the local Universal Transverse Mercator (UTM) projection. However,  $\theta_g$  reported by the AIS is given with respect to the WGS84 ellipsoidal coordinate

reference system. Therefore, a transformation is needed to compare the two directions.

A line of constant  $x$  in a local projection points to the grid north. Similarly, a line of equal longitude, i.e., a meridian, points to the true north. Along the central meridian in a UTM projection, grid north and true north coincide. The difference between the grid north and true north increases as the distance from a point to the central meridian

increases. The angle between the true north and the grid north is called the grid convergence (Osborne, 2013). For the spherical transverse Mercator projection, the convergence angle is given by (Osborne, 2013)

$$\gamma(\lambda, \phi) = \tan^{-1}(\tan(\lambda - \lambda_0) \sin \phi), \quad (17)$$

where  $\lambda$  and  $\phi$  denote longitude and latitude respectively. The longitude of the central meridian in the local projection is represented by  $\lambda_0$ . For example, Sentinel-2 imagery over the Strait of Gibraltar is given in UTM zone 30N. This zone has the central meridian at  $-3^\circ$ , hence  $\lambda_0 = -3^\circ$ . By substituting the ship's location into Eq. (17), the relevant convergence angle is found. Subsequently, the course through water can be corrected following

$$\theta_{w,global} = \theta_{w,local} - \gamma(\lambda, \phi). \quad (18)$$

The importance of the correction depends on the component of the estimated current. As shown in Section 2.4, the across-sailing-line component is much more sensitive to small changes in the angular difference between the two ship speed vectors, i.e.,  $\theta_g - \theta_w$ , than the along-sailing-line component.

Using Eqs. (11) and (12), we can compute that for a ship speed of  $10 \text{ m s}^{-1}$ , a typical grid convergence of  $2^\circ$  yields changes in the along- and across-sailing-line currents of about  $0.01 \text{ m s}^{-1}$  and  $0.35 \text{ m s}^{-1}$ , respectively. Clearly, the convergence angle needs to be corrected for especially in the case of the across-sailing-line component.

## 4. Data and methods

### 4.1. Study area

The Strait of Gibraltar was selected as a study area for four reasons: the abundance of ships, infrequent cloud cover, availability of HFR validation data and the presence of large surface currents. Surface currents in the strait are induced by several mechanisms, including a mean flow, barotropic tides, currents induced by internal waves and meteorological effects.

The density-driven mean flow in the strait consists of inflow of Atlantic fresh water at the surface and outflow of saltier water from the Mediterranean Sea at depth (e.g. Tsimplis and Bryden, 2000). The surface currents corresponding to this mean flow are of order  $1 \text{ m/s}$  (González et al., 2019). Additionally, barotropic tides contribute to surface currents, also reaching up to  $1 \text{ m/s}$ , with amplitudes decreasing eastward (e.g. Candela et al., 1990; González et al., 2019). Another notable feature of the Strait of Gibraltar are large-amplitude internal waves, generated by the interaction of the barotropic tide with the bottom topography in the strait (e.g. Vlasenko et al., 2009). These internal waves can also influence near-surface currents. For instance, Bruno et al. (2002) find  $> 0.5 \text{ m s}^{-1}$  modulations in eastward currents at  $20 \text{ m}$  depth. Notably, these internal waves have periods of less than  $30 \text{ min}$  (Ziegenbein, 1969; Vlasenko et al., 2009). This has two potential implications: first, it could introduce disagreement between validation data and our estimates given the hourly temporal resolution of the HFR data. Second, it may introduce an error in our estimates as we assume that the flow field is stationary during Kelvin wake generation, which takes several minutes.

### 4.2. Data

#### 4.2.1. Sentinel-2 imagery

All Sentinel-2 level 2A imagery covering the Strait of Gibraltar during July and August of 2021 was downloaded from the Copernicus Open Access Hub. This returned a collection of 25 images. For each image, the red, green and blue bands were averaged to produce a single greyscale image at  $10 \text{ m} \times 10 \text{ m}$  spatial resolution. Since there is a  $\sim 1 \text{ s}$  time delay between the blue and red bands (Binet et al., 2022), averaging of these bands can blur moving targets such as ocean waves. The advantage of averaging these bands is that pixel noise is slightly

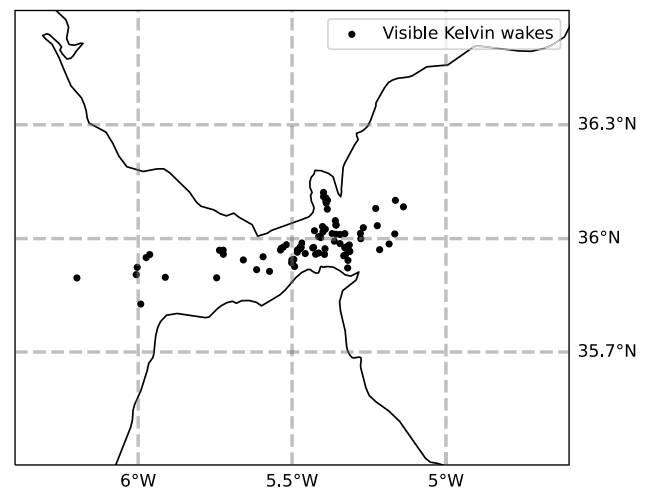


Fig. 7. Locations of the 81 Kelvin wakes in the Strait of Gibraltar that were visible on Sentinel-2 imagery during July and August 2021.

reduced, which can aid in the fitting process for weak Kelvin wake signals. In Appendix B we show that our main results remain unaltered by performing the analysis on any of the four individual  $10 \text{ m}$  resolution Sentinel-2 bands instead of averaging the RGB channels.

Subsequently, all images were manually scanned through to detect visible Kelvin wakes. A Kelvin wake was deemed visible if a signal corresponding to the Kelvin wake was visually present in the spectral domain. In 5 images, no visible Kelvin wakes were found. In the remaining 20 images, 81 visible Kelvin wakes were distinguished. Their locations are shown in Fig. 7. The Sentinel-2 images were manually cropped such that 81 images remained, each with a single Kelvin wake present.

#### 4.2.2. AIS data

AIS data covering the Strait of Gibraltar during July and August 2021 was provided by the Made Smart Group. The data was filtered for an interval of  $30 \text{ min}$  before and after the Sentinel-2 acquisition time. Subsequently, the data was filtered for ships sailing faster than  $5.6 \text{ m s}^{-1}$ , which corresponds to the minimum ship speed that generates Kelvin wakes that can be distinguished on Sentinel-2 imagery. Thereafter, the Maritime Mobile Service Identity (MMSI) number corresponding to each visible Kelvin wake was identified to couple each Kelvin wake with a time series of longitude, latitude,  $V_g$  and  $\theta_g$ . The mean longitude and latitude of this time series were set as the representative location of the estimated currents, while the average timestamp was chosen to be the representative time. These locations and timestamps were used for interpolation of validation datasets.

#### 4.2.3. HFR data

To validate the estimated surface currents, we used currents derived from High-Frequency Radar (HFR). An HFR transmits electromagnetic waves towards the sea surface. Some part of this signal will be scattered back to the radar through a mechanism called Bragg scattering (Lorente et al., 2017). The Doppler shift in this return signal is a measure of the surface current in the radar's line-of-sight. By measuring line-of-sight surface currents from multiple HFRs, total surface currents may be reconstructed. In the Strait of Gibraltar, three HFRs are operated by Puertos del Estado. Together, they provide hourly estimates of east- and northward components of surface currents in the Strait of Gibraltar, with a spatial resolution of approximately  $1 \times 1 \text{ km}$  (Lorente et al., 2017). Data from July and August of 2021 were downloaded from EMODnet-Physics. The spatial coverage of these HFRs was not sufficient to compute a surface current for each of the 81 datapoints. In 24 cases, the Kelvin wake was located outside of the spatial coverage of the HFR.

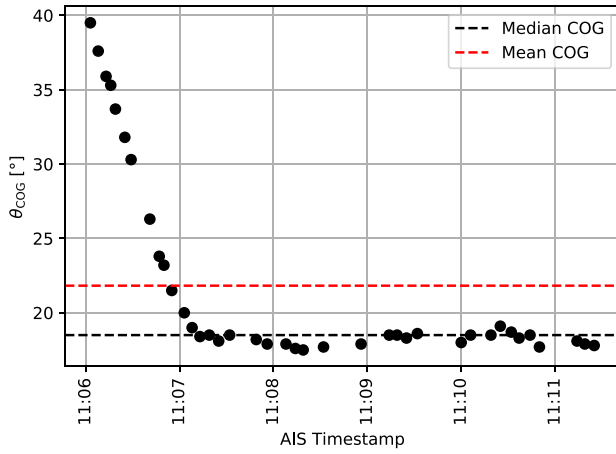


**Fig. 8.** Example of time series of  $\theta_g$  according to AIS data. The dashed red lines indicate the mean, while the dashed black lines denote the median level. (For interpretation of the references to colour in this figure legend, the reader is referred to the web version of this article.)

In another 4 cases, HFR data was missing at that particular day. Hence, only in 53 cases could the estimated surface currents be compared to the HFR-derived current.

In order to compare the HFR currents to the Sentinel-2+AIS estimates, they were linearly interpolated in time while nearest-neighbour interpolation was used in space. Thereafter, the east- and northward components were reprojected into the ship's frame of reference using

$$U_{\text{along}} = U_{\text{east}} \cos(\theta_w) + U_{\text{north}} \sin(\theta_w), \quad (19)$$

$$U_{\text{across}} = U_{\text{east}} \sin(\theta_w) - U_{\text{north}} \cos(\theta_w). \quad (20)$$

#### 4.2.4. CMEMS

A second source of validation data is provided by modelled currents from the Copernicus Marine Environment Monitoring Service (CMEMS). They provide a hydrodynamic model for the Mediterranean basin with a spatial resolution of  $4 \text{ km} \times 4 \text{ km}$ , temporal resolution of 15 min and 141 vertical levels (Clementi et al., 2021). Data were acquired from the Copernicus Marine Service. Since there was no missing data in space or time, all 81 Sentinel-2+AIS currents could be compared to the modelled currents. The same interpolation and reprojected as described for the HFR data was performed.

### 4.3. Methods

#### 4.3.1. Computation surface currents

For each Kelvin wake, a single value for  $V_g$  and  $\theta_g$  was needed to compute the surface currents. The AIS data provides time series of these variables. Therefore, representative values had to be extracted from the time series. In principle, the time series could be interpolated to the image acquisition time. However, a Kelvin wake is generated over several minutes. Therefore, the ship speed and course over this entire interval is relevant. AIS data points were selected to be relevant if they were spatially contained within the image of the Kelvin wake.

Subsequently, the median values of  $V_g$  and  $\theta_g$  were computed. The median was chosen over the mean since not all ships had a stationary speed and course. The median was generally able to capture the dominant speed and course along the length of the Kelvin wake. An example of a nonstationary time series of ship course is given in Fig. 8. Clearly, the course of the ship has changed over time, but the median is better able to retrieve the dominant direction during generation of the Kelvin wake.

Next,  $\hat{V}_w$  and  $\hat{\theta}_w$  were estimated using the fitting algorithm described in Section 3.2. To run the algorithm, candidate parameter sets

for  $V_w$  and  $\theta_w$  had to be defined. The  $V_g$  and  $\theta_g$  derived from AIS data were used to narrow the parameter set that had to be considered, which avoids unnecessary computations. This resulted in the following settings:

$$\begin{aligned} \theta_{w,\min} &= \theta_g - 20^\circ, & V_{w,\min} &= \max(6, V_g - 2) \text{ m s}^{-1}, \\ \theta_{w,\max} &= \theta_g + 20^\circ, & V_{w,\max} &= V_g + 2 \text{ m s}^{-1}, \\ \Delta\theta_w &= 0.1^\circ, & \Delta V_w &= 0.01 \text{ m s}^{-1}. \end{aligned} \quad (21)$$

The algorithm now returned the final two unknowns needed to estimate the surface current using Eqs. (1) and (2).

#### 4.3.2. Uncertainty quantification

We now had three independent datasets representing the same variable in space and time, hereafter referred to as the Sentinel-2+AIS, HFR and CMEMS datasets. For this situation, there exists a statistical technique called triple collocation to quantify the uncertainty associated to each individual dataset (Stoffelen, 1998). The method assumes that the three datasets can be represented as noisy linear transformations from the truth, i.e.,

$$y_i^n = \alpha_i + \beta_i x^n + \varepsilon_i, \quad (22)$$

where  $y_i^n$  represents the  $n$ th measurement of dataset  $i$  for  $i \in \{1, 2, 3\}$ , the  $\alpha$ 's and  $\beta$ 's represent calibration coefficients,  $x^n$  denotes the unknown truth and the  $\varepsilon$ 's represent additive Gaussian noise. It can be shown that (Gruber et al., 2016, Eq. 6)

$$\sigma_{\varepsilon_1}^2 = \sigma_1^2 - \frac{\sigma_{12}\sigma_{13}}{\sigma_{23}} = \sigma_1^2 \left( 1 - \frac{\rho_{12}\rho_{13}}{\rho_{23}} \right), \quad (23)$$

$$\sigma_{\varepsilon_2}^2 = \sigma_2^2 - \frac{\sigma_{12}\sigma_{23}}{\sigma_{13}} = \sigma_2^2 \left( 1 - \frac{\rho_{12}\rho_{23}}{\rho_{13}} \right), \quad (24)$$

$$\sigma_{\varepsilon_3}^2 = \sigma_3^2 - \frac{\sigma_{13}\sigma_{23}}{\sigma_{12}} = \sigma_3^2 \left( 1 - \frac{\rho_{13}\rho_{23}}{\rho_{12}} \right), \quad (25)$$

where  $\sigma_{\varepsilon_i}^2$  is the variance of the noise in dataset  $i$  and  $\sigma_i^2$  is the total variance in dataset  $i$  for  $i \in \{1, 2, 3\}$ .  $\sigma_{ij}$  is the covariance and  $\rho_{ij}$  is the correlation factor between dataset  $i$  and  $j$  for  $i, j \in \{1, 2, 3\}$  and  $i \neq j$ . These equations were used to compute two standard deviations per dataset; one standard deviation per component of the surface current.

## 5. Results

### 5.1. Surface current along sailing line

The correlations among the three datasets of surface currents along the sailing line are presented in Fig. 9. The strongest correlation is observed between the Sentinel-2+AIS estimates and HFR currents, with 95% of the variance explained by the linear fit. The corresponding Root-Mean-Square Error (RMSE) is  $0.21 \text{ m s}^{-1}$ , indicating a relatively small deviation between the two datasets. In comparison, the correlation between the Sentinel-2+AIS estimates and the CMEMS dataset explains 88% of the variance, albeit with a larger RMSE of  $0.35 \text{ m s}^{-1}$ . It is important to note that this comparison benefits from a larger sample size, as it is not affected by missing HFR data. Finally, the linear fit between the HFR and CMEMS datasets explains 87% of the variance, with a RMSE of  $0.24 \text{ m s}^{-1}$ . These results demonstrate a substantial level of agreement among all three datasets regarding the along-sailing-line surface currents.

### 5.2. Surface current across sailing line

In Fig. 10, the correlations between the three datasets for the across-sailing-line component of the surface current are displayed. The linear fit between the Sentinel-2+AIS and HFR datasets explains 76% of the variance, indicating a good level of agreement. However, there are now larger deviations between the two datasets, as evidenced by the

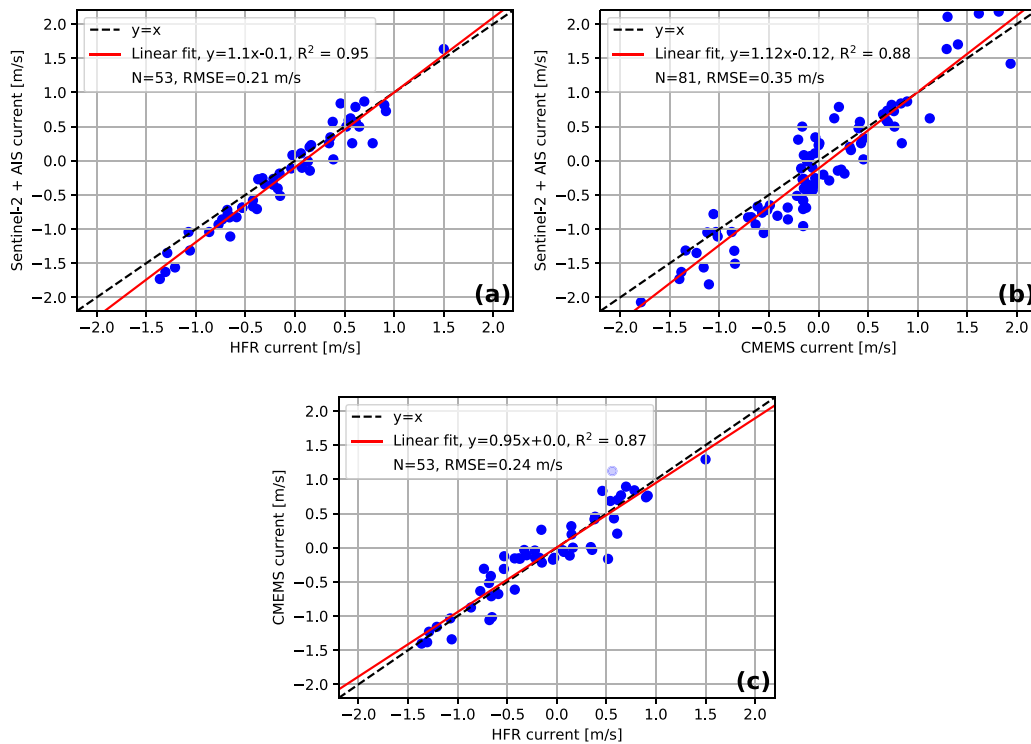


**Fig. 9.** Correlation between three datasets of along-sailing-line surface currents in the Strait of Gibraltar. (a) Sentinel-2+AIS vs. High-Frequency Radar (HFR). (b) Sentinel-2+AIS vs. numerical model CMEMS. (c) CMEMS vs. HFR.

RMSE of  $0.37 \text{ m s}^{-1}$ . The correlation between the Sentinel-2+AIS and CMEMS datasets reveals significant outliers, with only 49% of the variance explained. The RMSE between these two datasets is  $0.46 \text{ m s}^{-1}$ . Similarly, the fit between the HFR and CMEMS datasets explains 68% of the variance, with an RMSE of  $0.33 \text{ m s}^{-1}$ . Although there is still a clear correlation among all three datasets, these findings demonstrate that the agreement between the datasets for the across-sailing-line component of the surface current is weaker than for the along-sailing-line currents.

The lower accuracy observed in the across-sailing-line currents can be attributed to the increased sensitivity of this component to the angular difference between the ship speed vectors, as discussed in Section 2.4. In practice, ships do not sail in a straight line. Changes in ship course introduce uncertainties in  $\theta_g$ , which affect the accuracy of the across-sailing-line current estimates. To demonstrate the influence of course variability on the observed difference in accuracy between the along- and across-sailing-line components, we can filter out data points with the highest uncertainty in  $\theta_g$ . Here, we define  $\sigma_{\theta_g} = 1.4826\text{MAD}$ , where MAD represents the Median Absolute Deviation in the time series of  $\theta_g$  and the factor 1.4826 relates 50% of probability density to 68% of probability density for a normal distribution (e.g., Rousseeuw and Croux (1993)).

In Fig. 10, the data points corresponding to a  $\sigma_{\theta_g}$  value exceeding 2 degrees are highlighted in red. It can be observed that the red dots correspond to some of the largest outliers in the top two panels. However, in Fig. 10c, which contains no Sentinel-2+AIS data, the red dots no longer correspond to the largest outliers. This shows that the errors are inherent to the Sentinel-2+AIS dataset and are linked to the variability in  $\theta_g$ .

Upon removing these data points, the RMSE between the Sentinel-2+AIS and HFR datasets decreases from  $0.37 \text{ m s}^{-1}$  to  $0.24 \text{ m s}^{-1}$ . Hence, after filtering, the RMSE of the across-sailing-line currents is similar to the RMSE observed for the along-sailing-line component. A summary of error statistics before and after filtering out data points is given in Table 1.

**Table 1**

Error statistics of the estimated across-sailing-line surface currents between all three datasets.

Dataset 1	Dataset 2	Filter	N	$R^2$ [-]	RMSE [ $\text{m s}^{-1}$ ]	max [ $\text{m s}^{-1}$ ]
S2+AIS	HFR	–	53	0.76	0.37	0.88
S2+AIS	HFR	$\sigma_{\theta_g} < 2^\circ$	41	0.84	0.24	0.57
S2+AIS	CMEMS	–	81	0.49	0.46	1.38
S2+AIS	CMEMS	$\sigma_{\theta_g} < 2^\circ$	65	0.48	0.38	0.79
HFR	CMEMS	–	53	0.68	0.33	0.80
HFR	CMEMS	$\sigma_{\theta_g} < 2^\circ$	41	0.62	0.34	0.56

### 5.3. Total surface current

In Fig. 11, the estimated surface currents for two Sentinel-2 images are shown in the spatial domain. The red vectors correspond to the Sentinel-2+AIS estimates. The black vectors denote the currents derived from HFR, while the CMEMS modelled vector field is visualized by the blue vectors. There is generally good agreement in both magnitude and direction between the Sentinel-2+AIS and HFR currents. However, the CMEMS currents deviate most from the other two datasets, which is particularly noticeable in the northeastern part of both panels.

In addition, Fig. 11 also shows a clear limitation of the new measurement principle, i.e., it only produces a few point measurements per satellite image. In our case study, where 25 images were analysed, a total of 81 data points were obtained, resulting in an average of only three measurements per image. This quantity further reduces in regions with lower ship traffic and increased cloud cover. However, there are many data scarce regions in the world with dense shipping traffic where the proposed method could be beneficial.

### 5.4. Uncertainties

Uncertainties in the estimated along- and across-sailing-line surface currents were estimated using triple collocation, as described in Section 4.3.2. For the across-sailing-line component, the uncertainties

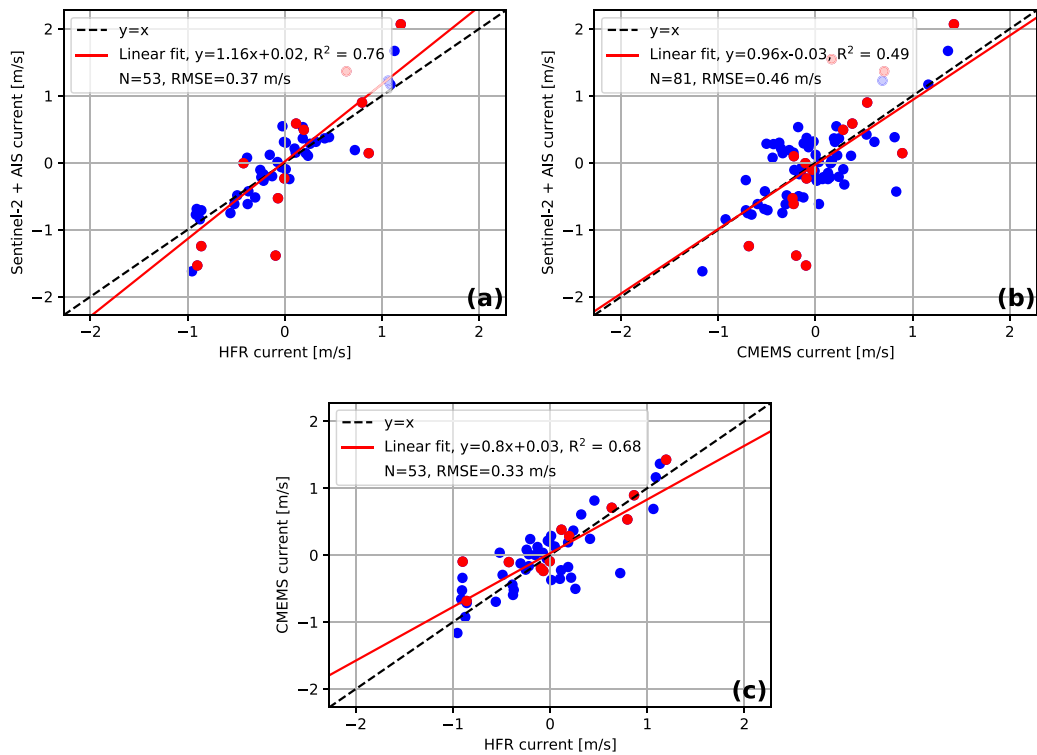


**Fig. 10.** Correlation between three datasets of across-sailing-line surface currents in the Strait of Gibraltar. In all figures, the red dots correspond to datapoints where  $\sigma_{\theta_g} > 2^\circ$ . (a) Sentinel-2+AIS vs. High-Frequency Radar (HFR). (b) Sentinel-2+AIS vs. numerical model CMEMS. (c) CMEMS vs. HFR. (For interpretation of the references to colour in this figure legend, the reader is referred to the web version of this article.)

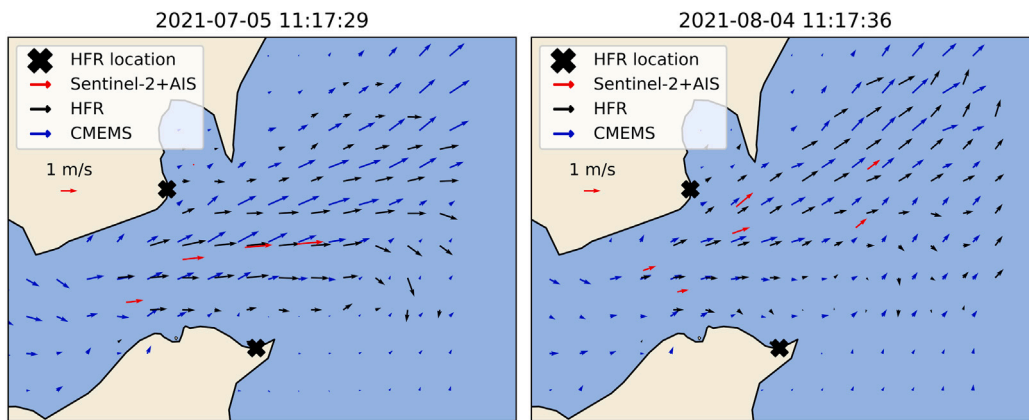


**Fig. 11.** Two examples of surface current fields in the Strait of Gibraltar. The red arrows visualize the estimated Sentinel-2+AIS surface currents, while the black arrows represent the vector field derived from High-Frequency Radar (HFR). The modelled currents from CMEMS are given by the blue vectors. The black crosses denote the locations of the HF radars. (For interpretation of the references to colour in this figure legend, the reader is referred to the web version of this article.)

were computed both before and after filtering for datapoints with  $\sigma_{\theta_g} < 2^\circ$ . The results are given in Table 2. Regarding the along-sailing-line component, the HFR data exhibited the lowest uncertainty with a standard deviation of  $0.09 \text{ m s}^{-1}$ . The Sentinel-2+AIS dataset ranked second with a standard deviation of  $0.14 \text{ m s}^{-1}$ . Finally, the CMEMS dataset had the largest uncertainty with a  $0.23 \text{ m s}^{-1}$  standard deviation.

For the across-sailing-line component, the HFR data once again demonstrated the highest accuracy, with a standard deviation of  $0.16 \text{ m s}^{-1}$ . The uncertainty in the Sentinel-2+AIS dataset increased considerably to  $0.30 \text{ m s}^{-1}$ , while the CMEMS data had a standard deviation of  $0.28 \text{ m s}^{-1}$ . However, after excluding the 12 datapoints with the largest variation in ship course, the standard deviation in the Sentinel-2+AIS dataset decreased from  $0.30 \text{ m s}^{-1}$  to  $0.16 \text{ m s}^{-1}$ . This reduction did not occur for the CMEMS dataset. We conclude that the Sentinel-2+AIS dataset provides accurate surface current estimates

in the absence of large variations in ship course, outperforming the modelled currents from CMEMS.

It should be noted that the sample sizes were relatively small, consisting only of 53 datapoints before filtering and 41 datapoints after filtering. According to Zwieback et al. (2012), the relative error in the estimated standard deviations is approximately  $\sqrt{\frac{5}{N}}$ , where  $N$  is the sample size. For  $N = 53$ , this yields a relative error of 0.31, indicating considerable uncertainty in the estimated standard deviations themselves. To achieve a relative error of less than 0.1, a sample size of 500 datapoints would be required.

## 6. Discussion and conclusion

The goal of this paper was to assess to what extent surface currents could be estimated using a new measurement principle involving the

**Table 2**

Estimated standard deviations for both surface current components using triple collocation. The right-most column gives standard deviations for the across-sailing-line surface currents after filtering for datapoints with  $\sigma_{\theta_g} < 2^\circ$ .

Dataset	Standard deviation [ $\text{m s}^{-1}$ ]		
	$U_{\text{along}}$	$U_{\text{across}}$	$U_{\text{across}}, \sigma_{\theta_g} < 2^\circ$
S2+AIS	0.14	0.30	0.16
HFR	0.09	0.16	0.16
CMEMS	0.23	0.28	0.29

vector difference between two ship speed vectors. We have shown that accurate surface current retrieval is possible, especially in the absence of large variability in ship course. The RMSEs of the along- and across-sailing-line components with respect to the HFR observations are  $0.21$  and  $0.24 \text{ m s}^{-1}$ , respectively, after filtering for ships with a large variability in ship course. These results demonstrate improved accuracy to the currents derived from AIS data alone by [Le Goff et al. \(2021\)](#), where the east- and north currents had RMSEs of  $0.38$  and  $0.28 \text{ m s}^{-1}$  with respect to data from drifting buoys. It is worth noting that their method provides average currents within a spatiotemporal interval of typically  $\frac{1}{8} - \frac{1}{4}^\circ$  spatial resolution and  $1 - 5$  days temporal resolution, making it suitable to study the average conditions of the flow field. In contrast, our method offers localized measurements in space and time, which could be valuable for the validation of hydrodynamic models.

Furthermore, our estimates exhibit a similar level of accuracy to both HFR and Sentinel-1 derived currents. [Lorente et al. \(2014\)](#) find RMSEs of  $0.21$  and  $0.20 \text{ m s}^{-1}$  for the east- and north currents from the HFRs with respect to in-situ data in the Strait of Gibraltar. Radial currents derived from Sentinel-1 had RMSEs of  $\sim 0.25 \text{ m s}^{-1}$  with respect to HFR-derived currents along the northern coast of Norway ([Moiseev et al., 2020](#)).

It is important to note that our case study focused solely on the Strait of Gibraltar. Nevertheless, we anticipate that the achieved accuracies would not significantly decline in other regions. In fact, we observed that ships in the Strait of Gibraltar exhibit greater variability in both speed and course compared to other regions. This variability represents a substantial source of error in the estimated surface currents. Consequently, we expect accuracy to potentially improve in regions where ships display less variability in speed and course.

Another point of discussion concerns the modulation of Kelvin wakes by other surface waves. Linear wave interactions should not impact the accuracy of the retrieval algorithm, as these interactions do not modify the wavelengths of the waves involved. Consequently, the shape and location of the Kelvin wake signal in the spectrum remain unaltered. However, as the surface slopes would be modulated, linear wave interactions do impact the visibility of the Kelvin wake on satellite imagery ([Liu et al., 2019](#)). Nonlinear wave interactions, which require very specific wavenumber combinations to occur, would only affect a specific direction in the Kelvin wake ([Zhu et al., 2008](#)). Since the proposed method integrates over the entire dispersion curve, we do not expect nonlinear interactions to alter the accuracy of the proposed method. Therefore, while ambient waves should not influence accuracy, they can have a considerable impact on the visibility of the Kelvin wake on satellite imagery.

The pushbroom imaging mechanism of Sentinel-2 could also introduce an error. As Sentinel-2 images are constructed row-by-row, there is a small time delay between successive rows of pixels. Such a time delay could elongate or compress dynamic targets such as waves. In [Appendix A](#) we derive an upper bound of  $0.025 \text{ m s}^{-1}$  for this error in case of fast ships sailing exactly along the satellite ground track. The error is even smaller for slower ships sailing at an angle from the satellite ground track. Hence, we conclude that this error can safely be neglected.

While our developed method demonstrates good accuracy, there are certain considerations regarding the potential measurement frequency.

First, the method relies on satellite imagery with temporal resolution on the order of days. Second, since the method relies on optical imagery, cloud cover further reduces the availability of useable imagery. Third, not all ships leave a visible Kelvin wake on satellite imagery. In our case study, approximately 25% of ships with  $V_g > 6 \text{ m s}^{-1}$  exhibited a visible Kelvin wake. This percentage aligns with the probabilities reported by [Liu and Deng \(2018\)](#), which range from 20% to 40% depending on ship type and satellite spatial resolution.

As a result of these limitations, measurements obtained using our method will be sparse in time. Still, the proposed measurement principle has several favourable features that demonstrate its potential to complement existing techniques. First, it is able to provide cost-effective data in regions that are not covered by traditional measurements such as buoys, surface drifters or HFRs. Specifically, whereas buoys are typically deployed outside of shipping lanes to avoid collisions, the Sentinel-2+AIS estimates directly provide information within these areas of large interest. Second, unlike SAR-based methods, two components of the surface current are provided and no prior knowledge on ambient waves is required. Third, the proposed method is able to estimate non-geostrophic currents, which is in contrast to satellite altimetry-derived currents.

To enhance the temporal resolution, additional high-resolution optical satellite imagery could be utilized, such as imagery provided by SPOT and Pléiades satellites, which offer higher spatial resolution compared to Sentinel-2. This would also decrease the minimum ship speed requirement of approximately  $6 \text{ m s}^{-1}$ , thereby increasing the number of visible Kelvin wakes. Additionally, higher resolution imagery might enable the application of the algorithm to ships navigating in inland waterways, where speeds are typically lower. In such shallower waters, it is important to consider local water depth as a factor.

Challenges related to cloud cover could be mitigated by considering the use of Synthetic Aperture Radar (SAR) imagery instead. Although Kelvin wakes have been reported to be visible on SAR imagery (e.g. [Lyden et al., 1988](#); [Graziano et al., 2016a](#)), the SAR imaging process causes waves to be distorted, mainly through the velocity bunching mechanism (e.g. [Hasselmann et al., 2013](#)). As a consequence, accurate retrieval of the ship speed may prove challenging as the shape of the observed spectral signal can deviate from the theoretical one.

For future work, it is worth considering the automation of Kelvin wake detection on imagery. In this study, Kelvin wakes were manually identified and extracted, which is a labour-intensive process. Automating this step allows for the analysis of larger datasets, enabling the presented method to generate a significant number of localized surface current measurements. These measurements can complement existing observational techniques, particularly in regions with dense shipping traffic.

#### CRedit authorship contribution statement

**Koen Haakman:** Writing – review & editing, Writing – original draft, Visualization, Validation, Software, Methodology, Investigation, Formal analysis, Data curation. **Martin Verlaan:** Writing – review & editing, Supervision, Resources, Project administration, Methodology, Funding acquisition, Conceptualization. **Avelon Gerritsma:** Writing – review & editing, Supervision, Methodology. **Arne van der Hout:** Writing – review & editing, Supervision, Conceptualization.

#### Declaration of competing interest

The authors declare that they have no known competing financial interests or personal relationships that could have appeared to influence the work reported in this paper.

#### Data availability

Data will be made available on request.

## Declaration of Generative AI and AI-assisted technologies in the writing process

During the preparation of this work the authors used ChatGPT 3.5 in order to improve readability of the manuscript. After using this tool/service, the authors reviewed and edited the content as needed and take full responsibility for the content of the publication.

## Acknowledgements

This work is funded through the Deltares Strategic Research Programme ‘Enabling Technologies’ and the Netherlands Organization for Scientific Research (ENW.GO.001.011). The authors would like to thank the Made Smart Group for providing the AIS data covering the Strait of Gibraltar.

## Appendix A. Potential error due to pushbroom mechanism

Sentinel-2’s MultiSpectral Instrument (MSI) is a pushbroom imager. Therefore, each image is constructed row-by-row as the platform moves across the scene. Consequently, there is a small time delay between successive rows of pixels. Such a time delay can distort dynamic targets such as waves. Here, we will quantify the worst-case error in our estimated surface currents due to this mechanism.

Suppose a wave with wavelength  $L$  is travelling exactly along the satellite ground track. Let  $T$  denote the time delay between two rows of pixels, which is approximately 1.57 ms according to the “LINE\_PERIOD” variable in the metadata of a Sentinel-2 file. Let  $\Delta t$  denote the imaging time delay between two successive wave crests. We have

$$\Delta t = \frac{LT}{10}, \quad (\text{A.1})$$

where the factor 10 is due to the pixel resolution. The length distortion of the wave,  $\Delta L$ , is given by the product of the wave’s phase speed  $c$ , and the imaging time delay  $\Delta t$ , i.e.,

$$\Delta L = c\Delta t. \quad (\text{A.2})$$

Now we substitute  $c = \sqrt{\frac{gL}{2\pi}}$  and Eq. (A.1) to find

$$\Delta L = \sqrt{\frac{gL}{2\pi}} \frac{LT}{10}. \quad (\text{A.3})$$

We are interested in the change in estimated ship speed  $\Delta V$  due to this distortion of the wavelength  $\Delta L$ . Let

$$\Delta V = \frac{dV}{dL} \Delta L, \quad (\text{A.4})$$

$$= \frac{g}{2\sqrt{2\pi}gL} \Delta L, \quad (\text{A.5})$$

where we have used that  $V = \sqrt{\frac{gL}{2\pi}}$ . Substitution of Eq. (A.3) yields

$$\Delta V = \frac{gL}{40\pi}. \quad (\text{A.6})$$

Clearly, the error would be largest for long, hence fast waves and for large time delays between successive rows of pixels. The longest ship waves in our case study were about 210 m. This yields an error in the ship velocity of  $0.025 \text{ m s}^{-1}$ . This directly translates to a  $0.025 \text{ m s}^{-1}$  error in the along-sailing-line current, while it has no impact on the across-sailing-line current.

Note that this value provides an upper bound for the error induced by the pushbroom mechanism. It assumes that waves are travelling exactly along the satellite ground track, while in practice, most sailing lines deviate from the satellite ground track. Moreover, most ships in our case study generated shorter waves ranging from 40 to 90 m, which further reduces the error. Therefore, we conclude that wave distortion due to the pushbroom mechanism can safely be ignored to estimate ship speeds from Kelvin waves on Sentinel-2 imagery.

## Appendix B. Supplementary data

Supplementary material related to this article can be found online at <https://doi.org/10.1016/j.rse.2024.114400>.

## References

- Binet, R., Bergsma, E., Poulain, V., 2022. Accurate SENTINEL-2 inter-band time delays. *ISPRS Ann. Photogram. Remote Sens. Spat. Inf. Sci.* V-1-2022, 57–66. <http://dx.doi.org/10.5194/isprs-annals-V-1-2022-57-2022>.
- Bruno, M., Juan Alonso, J., Cózar, A., Vidal, J., Ruiz-Cañavate, A., Echevarría, F., Ruiz, J., 2002. The boiling-water phenomena at camarinal sill, the strait of gibraltar. *Deep Sea Res. II: Top. Stud. Oceanogr.* 49, 4097–4113. [http://dx.doi.org/10.1016/S0967-0645\(02\)00144-3](http://dx.doi.org/10.1016/S0967-0645(02)00144-3), canary Islands, Azores, Gibraltar Observations (Canigo) Volume II : Studies of the Azores and Gibraltar regions.
- Candela, J., Winant, C., Ruiz, A., 1990. Tides in the strait of gibraltar. *J. Geophys. Res.: Oceans* 95, 7313–7335. <http://dx.doi.org/10.1029/JC095iC05p07313>.
- Chapron, B., Collard, F., Arduin, F., 2005. Direct measurements of ocean surface velocity from space: Interpretation and validation. *J. Geophys. Res.: Oceans* 110. <http://dx.doi.org/10.1029/2004JC002809>.
- Christodoulou, K., Herodotou, H., Michaelides, M.P., 2022. Estimation of sea surface current velocities using AIS data. In: 2022 23rd IEEE International Conference on Mobile Data Management. MDM, pp. 407–412. <http://dx.doi.org/10.1109/MDM55031.2022.00090>.
- Clementi, E., Aydogdu, A., Goglio, A.C., Pistoia, J., Escudier, R., Drudi, M., Grandi, A., Mariani, A., Lyubartsev, V., Lecci, R., Creti, S., Coppini, G., Masina, S., Pinardi, N., 2021. Mediterranean sea physical analysis and forecast (CMEMS MED-currents, EAS6 system) (version 1). [http://dx.doi.org/10.25423/CMCC/MEDSEA\\_ANALYSISFORECAST\\_PHY\\_006\\_013\\_EAS7](http://dx.doi.org/10.25423/CMCC/MEDSEA_ANALYSISFORECAST_PHY_006_013_EAS7).
- Gomit, G., Rousseaux, G., Chatellier, L., Calluau, D., David, L., 2014. Spectral analysis of ship waves in deep water from accurate measurements of the free surface elevation by optical methods. *Phys. Fluids* 26, 122101. <http://dx.doi.org/10.1063/1.4902415>.
- González, C.J., Reyes, E., Álvarez, Óscar, Izquierdo, A., Bruno, M., Mañanas, R., 2019. Surface currents and transport processes in the strait of gibraltar: Implications for modeling and management of pollutant spills. *Ocean Coast. Manage.* 179, 104869. <http://dx.doi.org/10.1016/j.ocecoaman.2019.104869>.
- Graziano, M., D’Errico, M., Rufino, G., 2016a. Ship heading and velocity analysis by wake detection in SAR images. *Acta Astronaut.* 128, 72–82. <http://dx.doi.org/10.1016/j.actaastro.2016.07.001>.
- Graziano, M., D’Errico, M., Rufino, G., 2016b. Wake component detection in X-band SAR images for ship heading and velocity estimation. *Remote Sens.* 8. <http://dx.doi.org/10.3390/rs8060498>.
- Gruber, A., Su, C.H., Zwieback, S., Crow, W., Dorigo, W., Wagner, W., 2016. Recent advances in (soil moisture) triple collocation analysis. *Int. J. Appl. Earth Obs. Geoinf.* 45, 200–211. <http://dx.doi.org/10.1016/j.jag.2015.09.002>.
- Hasselmann, K., Chapron, B., Aouf, L., Arduin, F., Collard, F., Engen, G., Hasselmann, S., Heimbach, P., Johnsen, H., Krogstad, H., Lehner, S., Li, J.G., Li, X.M., Rosenthal, W., Schulz-Stellenfleth, J., 2013. The ERS SAR wave mode: A breakthrough in global ocean wave observations. In: *ERS Missions: 20 Years of Observing Earth*. ESA/ESTEC, pp. 165–198.
- Hauser, D., Abdalla, S., Arduin, F., Bidlot, J.R., Bourassa, M., Cotton, D., Gommenginger, C., Evers-King, H., Johnsen, H., Knaff, J., Lavender, S., Mouche, A., Reul, N., Sampson, C., Steele, E.C., Stoffelen, A., 2023. Satellite remote sensing of surface winds, waves, and currents: Where are we now? *Surv. Geophys.* 44, 1357–1446. <http://dx.doi.org/10.1007/s10712-023-09771-2>.
- Isern-Fontanet, J., Ballabrera-Poy, J., Turiel, A., García-Ladona, E., 2017. Remote sensing of ocean surface currents: a review of what is being observed and what is being assimilated. *Nonlinear Process. Geophys.* 24, 613–643. <http://dx.doi.org/10.5194/npg-24-613-2017>.
- Klemas, V., 2012. Remote sensing of coastal and ocean currents: An overview. *J. Coast. Res.* 28, 576–586. <http://dx.doi.org/10.2112/JCOASTRES-D-11-00197.1>.
- Le Goff, C., Boussidi, B., Mironov, A., Guichoux, Y., Zhen, Y., Tandeo, P., Gueguen, S., Chapron, B., 2021. Monitoring the greater agulhas current with AIS data information. *J. Geophys. Res.: Oceans* 126, e2021JC017228. <http://dx.doi.org/10.1029/2021JC017228>.
- Liu, Y., Deng, R., 2018. Ship wakes in optical images. *J. Atmos. Ocean. Technol.* 35, 1633–1648. <http://dx.doi.org/10.1175/JTECH-D-18-0021.1>.
- Liu, Y., Deng, R., Zhao, J., 2019. Simulation of kelvin wakes in optical images of rough sea surface. *Appl. Ocean Res.* 89, 36–43. <http://dx.doi.org/10.1016/j.apor.2019.05.006>.
- López-Dekker, P., Rott, H., Prats-Iraola, P., Chapron, B., Scipal, K., de Witte, E., 2019. Harmony: an earth explorer 10 mission candidate to observe land, ice, and ocean surface dynamics. In: *IGARSS 2019-2019 IEEE International Geoscience and Remote Sensing Symposium*. pp. 8381–8384. <http://dx.doi.org/10.1109/IGARSS.2019.8897983>.
- Lorente, P., Piedracoba Varela, S., Soto-Navarro, J., Ruiz, M., Álvarez Fanjul, E., Montero, P., 2017. The high-frequency coastal radar network operated by Puertos del Estado (Spain): Roadmap to a fully operational implementation. *IEEE J. Ocean. Eng.* 42, 56–72. <http://dx.doi.org/10.1109/JOE.2016.2539438>.

- Lorente, P., Soto-Navarro, J., Fanjul, E.A., Piedracoba, S., 2014. Accuracy assessment of high frequency radar current measurements in the Strait of Gibraltar. *J. Oper. Oceanogr.* 7, 59–73. <http://dx.doi.org/10.1080/1755876X.2014.11020300>.
- Luengo Hendriks, C., Ginkel, M.v., Verbeek, P., Vliet, L.v., 2005. The generalized radon transform: Sampling, accuracy and memory considerations. *Pattern Recognit.* 38, 2494–2505. <http://dx.doi.org/10.1016/j.patcog.2005.04.018>.
- Lumpkin, R., Özgökmen, T., Centurioni, L., 2017. Advances in the application of surface drifters. *Annu. Rev. Mar. Sci.* 9, 59–81. <http://dx.doi.org/10.1146/annurev-marine-010816-060641>.
- Lyden, J.D., Hammond, R.R., Lyzenga, D.R., Shuchman, R.A., 1988. Synthetic aperture radar imaging of surface ship wakes. *J. Geophys. Res.: Oceans* 93, 12293–12303. <http://dx.doi.org/10.1029/JC093iC10p12293>.
- Moiseev, A., Johnsen, H., Hansen, M.W., Johannessen, J.A., 2020. Evaluation of radial ocean surface currents derived from sentinel-1 iw doppler shift using coastal radar and lagrangian surface drifter observations. *J. Geophys. Res.: Oceans* 125, e2019JC015743. <http://dx.doi.org/10.1029/2019JC015743>.
- Osborne, P., 2013. The Mercator Projections. Edinburgh, Zenodo, <http://dx.doi.org/10.5281/zenodo.35392>.
- Romeiser, R., Suchandt, S., Runge, H., Steinbrecher, U., Grunler, S., 2010. First analysis of terrasar-x along-track insar-derived current fields. *IEEE Trans. Geosci. Remote Sens.* 48, 820–829. <http://dx.doi.org/10.1109/TGRS.2009.2030885>.
- Rousseeuw, P., Croux, C., 1993. Alternatives to the median absolute deviation. *J. Amer. Statist. Assoc.* 88, 1273–1283. <http://dx.doi.org/10.1080/01621459.1993.10476408>.
- Stoffelen, A., 1998. Toward the true near-surface wind speed: Error modeling and calibration using triple collocation. *J. Geophys. Res.: Oceans* 103, 7755–7766. <http://dx.doi.org/10.1029/97JC03180>.
- Sun, Y., Liu, P., Jin, Y., 2018. Ship wake components: Isolation, reconstruction, and characteristics analysis in spectral, spatial, and TerraSAR-X image domains. *IEEE Trans. Geosci. Remote Sens.* 56, 4209–4224. <http://dx.doi.org/10.1109/TGRS.2018.2828833>.
- Tsimplis, M., Bryden, H., 2000. Estimation of the transports through the strait of gibraltar. *Deep Sea Res. I: Oceanogr. Res. Pap.* 47, 2219–2242. [http://dx.doi.org/10.1016/S0967-0637\(00\)00024-8](http://dx.doi.org/10.1016/S0967-0637(00)00024-8).
- Tunaley, J., 2003. The estimation of ship velocity from SAR imagery. In: *IGARSS 2003. 2003 IEEE International Geoscience and Remote Sensing Symposium. Proceedings (IEEE Cat. No. 03CH37477)*. pp. 191–193. <http://dx.doi.org/10.1109/IGARSS.2003.1293720>.
- Vlasenko, V., Garrido, J.C.S., Stashchuk, N., Lafuente, J.G., Losada, M., 2009. Three-dimensional evolution of large-amplitude internal waves in the strait of gibraltar. *J. Phys. Oceanogr.* 39, 2230–2246. <http://dx.doi.org/10.1175/2009JPO4007.1>.
- Yiew, L.J., Magee, A.R., 2022. Deriving tidal currents from AIS data. *J. Phys. Conf. Ser.* 2311, 012003. <http://dx.doi.org/10.1088/1742-6596/2311/1/012003>.
- Yurovskaya, M., Kudryavtsev, V., Chapron, B., Collard, F., 2019. Ocean surface current retrieval from space: The sentinel-2 multispectral capabilities. *Remote Sens. Environ.* 234, 111468. <http://dx.doi.org/10.1016/j.rse.2019.111468>.
- Zhu, Q., Liu, Y., Yue, D.K.P., 2008. Resonant interactions between kelvin ship waves and ambient waves. *J. Fluid Mech.* 597, 171–197. <http://dx.doi.org/10.1017/S002211200700969X>.
- Ziegenbein, J., 1969. Short internal waves in the strait of gibraltar. *Deep Sea Res. Oceanogr. Abstr.* 16, 479–487. [http://dx.doi.org/10.1016/0011-7471\(69\)90036-9](http://dx.doi.org/10.1016/0011-7471(69)90036-9).
- Zilman, G., Zapolski, A., Marom, M., 2004. The speed and beam of a ship from its wake's SAR images. *IEEE Trans. Geosci. Remote Sens.* 42, 2335–2343. <http://dx.doi.org/10.1109/TGRS.2004.833390>.
- Zwieback, S., Scipal, K., Dorigo, W., Wagner, W., 2012. Structural and statistical properties of the collocation technique for error characterization. *Nonlinear Process. Geophys.* 19, 69–80. <http://dx.doi.org/10.5194/npg-19-69-2012>.